Phase competition in HfO_2 with applied electric field from first principles

Y. Qi and Karin M. Rabe
Department of Physics & Astronomy, Rutgers University, Piscataway, New Jersey 08854, USA

(Received 18 September 2020; accepted 12 November 2020; published 11 December 2020)

In this work, the results of first-principles density-functional-theory calculations are used to construct the energy landscapes of HfO_2 and its Y and Zr substituted derivatives as a function of symmetry-adapted lattice-mode amplitudes. These complex energy landscapes possess multiple local minima, corresponding to the tetragonal, oIII ($Pca2_1$), and oIV ($Pmn2_1$) phases. We find that the energy barrier between the nonpolar tetragonal phase and the ferroelectric oIII phase can be lowered by Y and Zr substitution. In $Hf_{0.5}Zr_{0.5}O_2$ with an ordered cation arrangement, Zr substitution makes the oIV phase unstable, and it becomes an intermediate state in the tetragonal to oIII phase transition. Using these energy landscapes, we interpret the structural transformations and hysteresis loops computed for electric-field cycles with various choices of field direction. The implications of these results for interpreting experimental observations, such as the wake-up and split-up effects, are also discussed. These results and analysis deepen our understanding of the origin of ferroelectricity and field cycling behaviors in HfO_2-based films and allow us to propose strategies for improving their functional properties.

DOI: 10.1103/PhysRevB.102.214108

I. INTRODUCTION

Hafnia (HfO_2) has long been recognized as a high-κ material, valuable in complementary metal-oxide-semiconductor (CMOS) applications [1,2]. In 2011, Si-doped HfO_2 thin films under mechanically encapsulated crystallization were observed to be ferroelectric [3], which led to a renewal of scientific interest and much recent theoretical and experimental research [3–11].

HfO_2 is a binary oxide with a number of polymorphs. At high temperatures ($T > 2900$ K), bulk HfO_2 has a high-symmetry $Fm\bar{3}m$ cubic fluorite structure, in which each Hf atom is located at the center of an oxygen cube [Fig. 1(a)]. As the temperature decreases (2900 K $> T >$ 2073 K) [12], this cubic structure becomes unstable. In this temperature range, the oxygen atoms displace in a X_2^- mode pattern [Fig. S1(a)] to give a tetragonal $P4_2/nmc$ structure [Fig. 1(b)] in which four Hf-O bonds become slightly shorter while the other four become slightly longer [13]. Below 2073 K, bulk HfO_2 is found in a $P2_1/c$ monoclinic phase, in which additional distortions reduce the coordination number of Hf from 8 to 7. However, all these known bulk phases are centrosymmetric and thus nonpolar. The ferroelectricity observed in HfO_2 thin films is attributed to an orthorhombic $Pca2_1$ (denoted by oIII) phase with polarization along [001], as has been confirmed by both experimental and theoretical studies [11,13–16]. A competing [011]-polarized orthorhombic $Pnm2_1$ (denoted by oIV) phase [Fig. 1(d)] has been proposed on the basis of first-principles calculations [16] but has not yet been experimentally reported. These facts indicate that HfO_2 has a complex energy landscape with multiple local minima. Investigating the state switching between different local minima, especially switching driven by an electric field, is of great importance in understanding the origin of ferroelectricity and the behavior in applied electric fields.

In this paper, we report the results of first-principles calculations for HfO_2 and substitutional derivatives (Y-doped HfO_2 and $Hf_{0.5}Zr_{0.5}O_2$), with the construction of their energy landscapes as a function of selected symmetry-adapted lattice modes. Specifically, we consider uniform electric fields applied in various directions with respect to the crystal axes and map out the structural evolution and hysteresis loops for selected electric field profiles. We find that Y and Zr substitution modifies the energy landscape of pure HfO_2. In particular, the substitutions change the minimum-barrier path from the nonpolar tetragonal to the ferroelectric oIII phase and between up and down ferroelectric variants. These results lead to a better understanding of wake-up and switching behavior in these systems, enabling electric-field control of competing phases in HfO_2 and its derivatives.

II. METHODS

We carry out density functional theory (DFT) calculations with the QUANTUM ESPRESSO [17] package for structural relaxations under finite electric fields and the ABINIT [18] package for structure optimizations with fixed lattice modes. Optimized norm-conserving local density approximation (LDA) pseudopotentials were generated using the OPIUM package [19,20]. A $4 \times 4 \times 4$ Monkhorst-Pack k-point mesh was used to sample the Brillouin zone for the conventional 12-atom cell with corresponding meshes for the supercells. The plane-wave cutoff energy was 50 Ry [21]. Structural relaxations were performed with a force threshold of 5.0×10^{-6} Hartree per Bohr. Relaxed structural parameters for the various bulk phases of pure HfO_2 are reported in Supplemental Material (SM) section I [22]. The computed lattice constants are identical to those in our previous work [13] and are in good agreement with the results in other studies.

 ©2020 American Physical Society

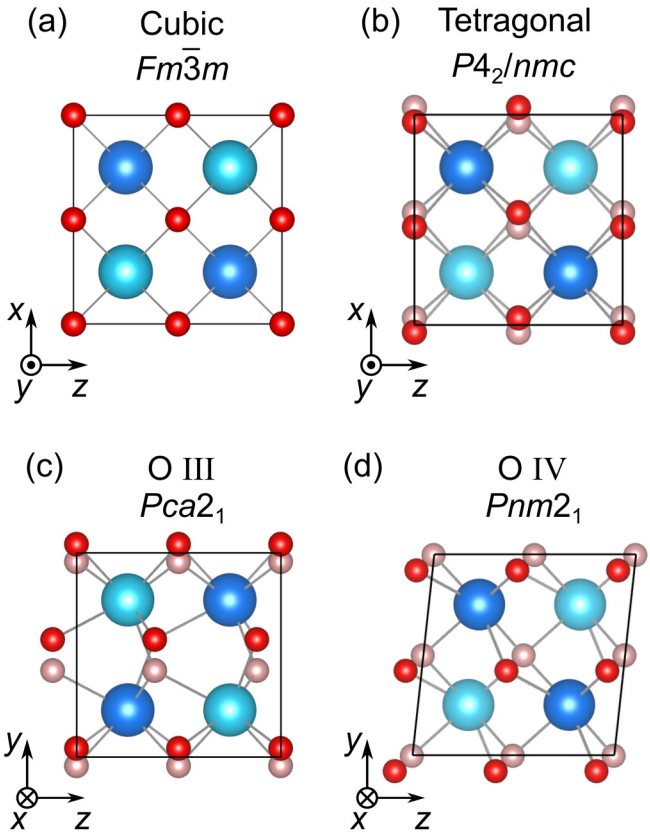

FIG. 1. (a) Cubic, (b) tetragonal, (c) oIII, and (d) oIV phases of HfO_2. Along the viewing direction, nearer and farther Hf atoms are represented by dark blue and light blue spheres, respectively. Similarly, nearer and farther O atoms are represented by red and pink spheres, respectively.

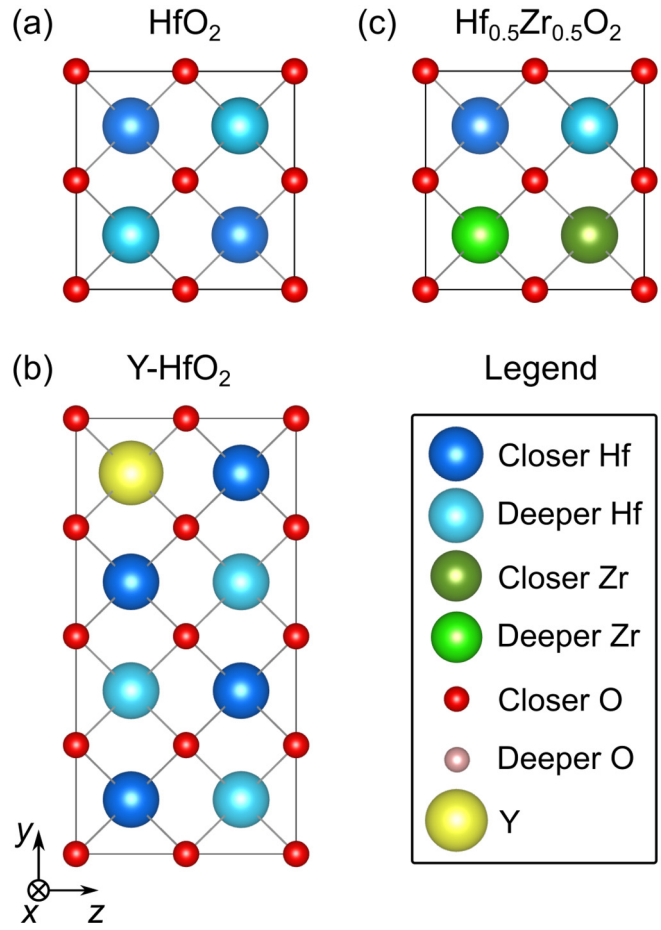

FIG. 2. High-symmetry cubic structures of the (a) bulk HfO_2, (b) Y-doped HfO_2, and (c) $Hf_{0.5}Zr_{0.5}O_2$ unit cells. Hf, Zr, O, and Y atoms are represented by blue, green, red, and yellow spheres respectively. As in Fig. 1, the darkness of the color indicates the spatial distance along the view direction; closer atoms are represented by dark colors, while farther ones are represented by light colors.

Here, we consider pure HfO_2 and two substitutional derivatives: Y-doped HfO_2 (Y-HfO_2) and $Hf_{0.5}Zr_{0.5}O_2$, as shown in Fig. 2. The conventional unit cell of pure HfO_2 contains 12 atoms or 4 formula units [Fig. 2(a)]. For Y-HfO_2, we double this unit cell along the y axis and substitute one of the Hf atoms by a Y atom, corresponding to a 12.5% doping concentration [Fig. 2(b)]. For $Hf_{0.5}Zr_{0.5}O_2$, we consider a structure with 1:1 layered cation ordering, as shown in Fig. 2(c). Previous experimental work has shown that this superlattice structure with alternating Zr and Hf cation layers exhibits electrical behavior quite similar to that of random-cation $Hf_{0.5}Zr_{0.5}O_2$ [23].

We describe the low-symmetry structures in each system by homogeneously straining them back to the lattice of the ideal cubic fluorite reference structure and decomposing the atomic displacements from the reference structure into the symmetry-adapted lattice modes of the reference structure [11,13]. The atomic displacement patterns of the lattice modes and the method for calculating the mode amplitudes are described in SM Sec. II [22]. In Table S6, the lattice-mode patterns and amplitudes relevant to the optimized tetragonal, oIII, and oIV phases are listed. The oxygen atom positions in the tetragonal structure are obtained from an antipolar X_2^- mode, with displacements of oxygen chains along the fourfold direction, here taken as the x direction, alternating in a 2D checkerboard pattern [Fig. S1(a)]. Starting from the tetragonal structure, the polar phases are generated by the threefold-degenerate zone-center polar Γ_4^- mode, corresponding to uniform displacement of the Hf atoms relative to the simple cubic oxygen network [Fig. S1(c)]. We refer to these modes as Γ_x, Γ_y, and Γ_z, with amplitudes u_x, u_y, and u_z, respectively. The oIII structure, whose polarization is along the [001] direction, has only one nonzero polar mode amplitude $u_z \neq 0$. In the oIV structure, $u_y = u_z \neq 0$, indicating a [011]-directed polarization.

There are two relevant components of the antipolar X_5^+ mode. The $X_{5,y}^+(\boldsymbol{q} \parallel \hat{\boldsymbol{x}})$ mode, with amplitude A_y, describes the displacement of oxygen layers along the y axis, alternating in the x direction, as shown in Fig. S1(d). This amplitude is nonzero both in the oIII and oIV structures. The $X_{5,z}^+(\boldsymbol{q} \parallel \hat{\boldsymbol{y}})$ mode, with amplitude B_z, describes the displacement of oxygen layers along the z axis, alternating in the y direction, as shown in Fig. S1(c). This amplitude is nonzero only in the oIII structure. B_z and u_z combine to give zero and nonzero oxygen displacements in alternating layers in the oIII structure.

For constructing the energy landscape as a function of the lattice-mode amplitudes, we generate structures with

selected amplitudes of the lattice modes, and then, by using the ABINIT package, relax the structures with the constraint that the selected mode amplitudes stay fixed while the amplitudes of other modes compatible with the resulting symmetry are optimized (SM Sec. III [22]). In certain cases to be discussed below, when the lattice mode amplitude is zero, the structure is relaxed with the lower symmetry corresponding to a small nonzero value of the lattice mode amplitude. This ensures that the energy plotted as a function of lattice amplitude is continuous through zero amplitude, which would not in general be the case if the zero-amplitude energy were computed at a saddle point protected by high symmetry. Then, we fit the calculated energies with Landau polynomials with the lattice-mode amplitudes as order parameters and use the polynomials to generate the energy landscapes.

We determine the effects of uniform applied electric field by relaxing the structure with added forces $\boldsymbol{F}_i$ on the ions: $\boldsymbol{F}_i = Z_i^* e \cdot \boldsymbol{E}$, where Z_i^* is the effective charge tensor of ion i and $\boldsymbol{E}$ is the applied electric field (SM Sec. III [22]). Previous studies have shown that this "force method" for the simulation of the effect of nonzero electric field gives consistent results with direct first-principles calculations including finite nonzero electric field [24–26]. To construct electric-field hysteresis loops, an electric field cycle is applied to each of the systems considered with the tetragonal structure as the initial state. In each cycle, we fix a direction for the electric field and then increase the magnitude of the electric field in steps from 0 to $+E_{\max}$ in steps, then decrease it to $-E_{\max}$, and then increase it again to $+E_{\max}$. Here, $E_{\max} = 15.5$ MV/cm is the maximum electric field that the HfO_2 crystal can sustain in our DFT calculations. Beyond $E_{\max} = 15.5$ MV/cm, the system becomes ionically conductive. The step size is $\Delta E = 1.5$ MV/cm, except near the critical electric field at which switching occurs, where ΔE is reduced to 0.5 MV/cm. The effective charge tensor Z_i^* is recalculated at each step (SM Sec. III [22]). For each value of E, the optimized structure from the previous step is used as the starting structure for relaxation. Hysteresis loops are plotted showing the polar-mode amplitudes of the optimized structures as a function of electric field.

The lattice-mode-amplitude energy landscape can be used to understand the electric-field cycling behaviors to first order in the field. To see this, we start with a given nonzero electric field and relax the structure as described above. Next, the resulting structure is relaxed at zero field, constraining the values of u_y and u_z, to determine one point in the lattice-mode-amplitude energy landscape. We find that the amplitudes of the nonpolar modes in the structure relaxed under a nonzero electric field, and in the structure computed with a zero electric field and constrained values of u_y and u_z, are the same to a good approximation. Therefore, the effect of nonzero field can be described by adding a term $-P{\cdot}E$, where P is the spontaneous polarization [27], to the computed zero-field energy landscape.

III. RESULTS

We begin by considering the energy landscape of pure HfO_2 in zero applied field, identifying the local minima that correspond to competing phases and analyzing the barriers that separate them. We then present results for electric-field hysteresis loops of pure HfO_2, focusing on the structural changes and switching behavior as the magnitude of the field changes. Finally, we extend our discussion to the Y-HfO_2 and $Hf_{0.5}Zr_{0.5}O_2$ systems, and show how Y and Zr substitutions change the energy landscape and electric-field cycling behaviors.

A. Pure HfO_2

The energy landscape of pure HfO_2 as a function of the two polar mode amplitudes u_y and u_z is shown in Fig. 3(a). There are three types of local minima, corresponding to the tetragonal, oIII, and oIV phases. The optimal path from the tetragonal phase to the oIII phase runs along the horizontal axis, with the optimal value of u_y at each u_z being zero. Similarly, the optimal path from the tetragonal phase to the oIV phase runs along the line $u_y = u_z$.

The nature of the barriers between the local minima can be understood by plotting the energy and the relaxed amplitudes A_y and B_z of the X_5^+ modes (Fig. S1) for two straight-line paths in (u_z, u_y) space, as shown in Figs. 3(b) and 3(c). Along the straight line path $(u, 0^+)$ [Fig. 3(b)], a cusp at $u = 0.12$ Å separates the two local minima corresponding to the tetragonal and oIII phases, with a change in space group symmetry from $Aba2$, for the tetragonal phase with a constrained polar distortion, to $Pca2_1$, for the oIII phase. In the $Aba2$ phase, the mode amplitude A_y grows linearly with u, while B_z remains zero [Fig. 3(b) and Fig. S1(b)]. In the $Pca2_1$ phase, found for $u > 0.12$ Å, $A_y \approx B_z \neq 0$, with jumps in both A_y and B_z across the cusp. The jump in B_z can be understood by plotting the energy landscape as a function of u_z and B_z, with other symmetry-allowed modes, including A_y, allowed to relax [Fig. 4(a)]. For $u_z < 0.12$ Å, the energy as a function of B_z has a single minimum at $B_z = 0$, while for $u_z > 0.12$ Å, it is a double well [Fig. 4(b)].

To understand the nature of the barrier between the tetragonal phase and the oIV phase, we show the energy and the mode amplitudes A_y and B_z as a function of u along the straight-line path (u, u) connecting the tetragonal phase to the oIV phase [Fig. 3(b)]. Nonzero u lowers the symmetry to $Pnm2_1$. With increasing u, A_y grows linearly with u_z and B_z remains zero. The $Pnm2_1$ oIV phase is metastable, with an energy of 31 meV/f.u. above the tetragonal phase. The energy barrier from the oIV phase is only 6 meV/f.u. and is smooth rather than cusplike.

To investigate the electrical field cycling behavior, we applied two electric field cycles to the tetragonal phase, one with electric field along the [001] direction and the other along [011]. The polar-mode-amplitude hysteresis loops are shown in Fig. 5(a) and the evolution of the free energy landscape with electric field is shown in Figs. S5. For $\boldsymbol{E}$//[001], a tetragonal to polar oIII phase transition occurs at $E_{\mathrm{T}\to\mathrm{P}} = 15.0$ MV/cm. After the electric field is returned to zero, the system is trapped at the local minimum corresponding to the oIII structure. Here, we do not observe the polar distortion switching under any negative electric field with a magnitude below $E_{\max}$, because of the large energy barrier separating the local minima corresponding to the [001] and [00$\bar{1}$] polarized oIII structures. For $\boldsymbol{E}$//[011], the critical field for inducing a

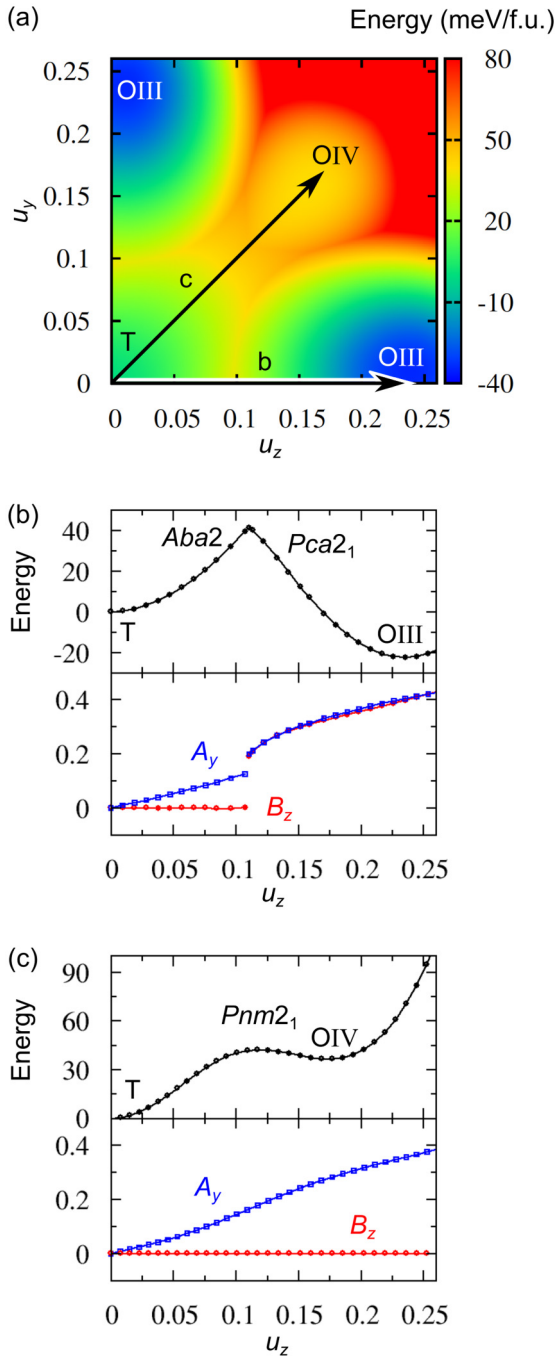

FIG. 3. (a) Energy landscape of HfO_2 as a function of u_y and u_z; we focus on the two paths indicated by the arrows. (b) Energy, A_y, and B_z as a function of u along the path b from the tetragonal to the oIII phase. Dots are calculated points and the solid line is an interpolation. (c) Energy, A_y, and B_z as a function of u along the path c from the tetragonal to the oIV phase.

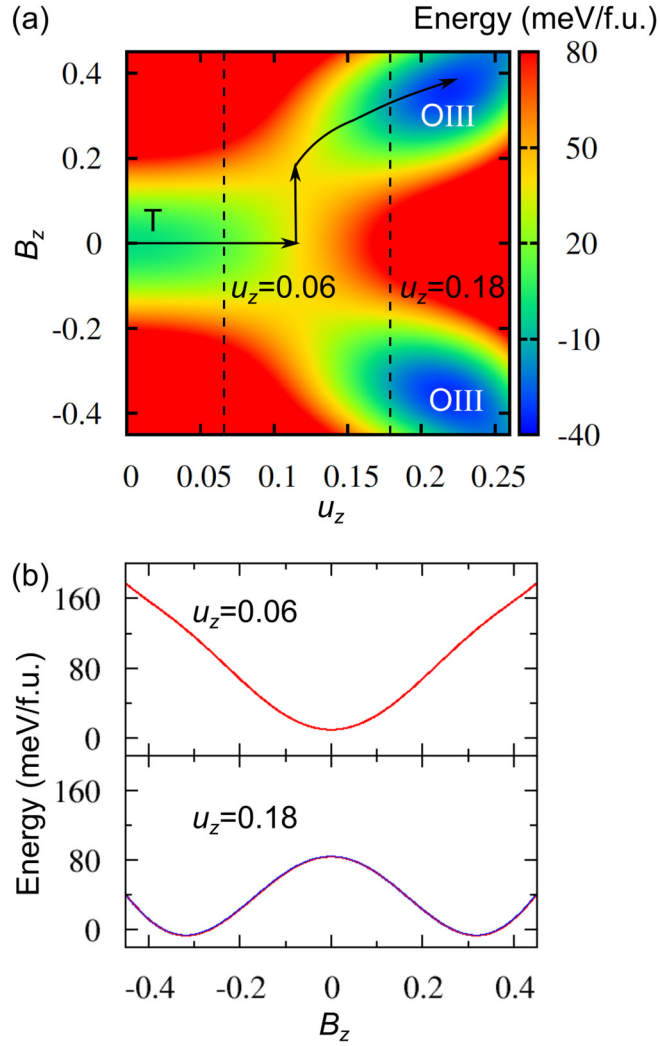

FIG. 4. (a) Energy landscape of HfO_2 as a function of u_z and B_z. (b) Energy as a function of B_z, for u_z smaller and larger than the critical value 0.12 Å, respectively.

tetragonal to polar oIV phase transition is $E_{T\to P} = 6$ MV/cm. After the electric field is returned to zero, the system is trapped at the local minimum corresponding to the oIV structure. As the electric field becomes more negative, this local minimum disappears and at $E_{P\to T} = -3.0$ MV/cm, the system switches back to the tetragonal phase. With further increase of the electric field in the negative direction, the polar distortion switches at $E_{T\to -P} = -6$ MV/cm.

B. Y-HfO_2

The Y-doped HfO_2 $1 \times 2 \times 1$ supercell is shown in Fig. 2(b). The arrangement of Y atoms considered respects tetragonal symmetry, so that relaxing the structure from the high-symmetric cubic phase gives rise to a nonpolar tetragonal structure quite similar to the tetragonal structure of HfO_2, with nonzero values for the X_2^- mode. Here, we would like to note that for the phases we study, we find that heterovalent Y doping adds a hole at the top of the valence band without introducing any states in the gap, which is consistent with Ref. [28].

The energy of Y-HfO_2 as a function of u_z is shown in Fig. 6(a), where we see three phases separated by cusps, with one local minimum at $u_z = 0$ Å and a second at $u_z = 0.17$ Å. Relative to pure HfO_2, both the value of u_z at the first cusp and the height of the energy barrier separating the two local minima are lower in Y-HfO_2. For values of u_z below the

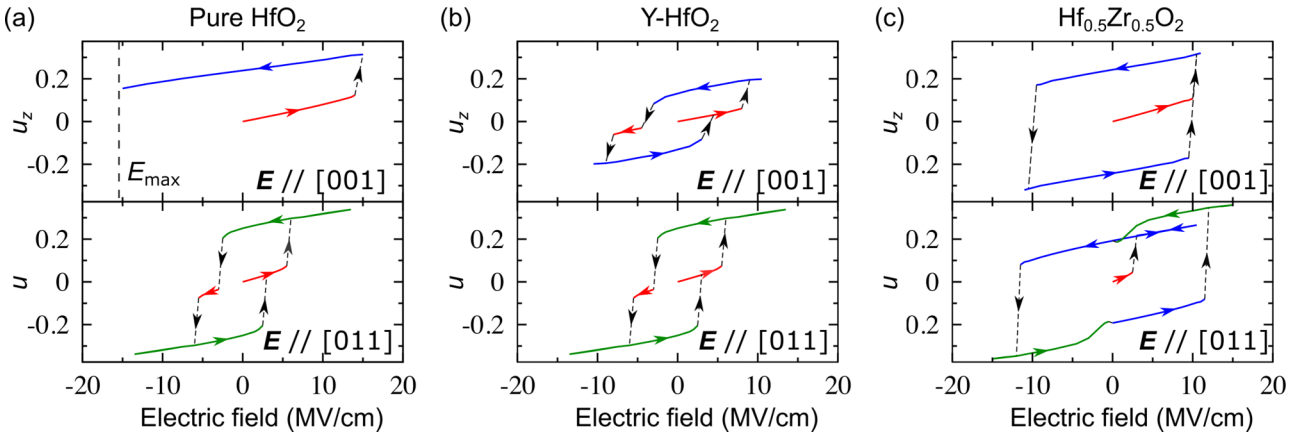

FIG. 5. Hysteresis loops of (a) pure HfO_2, (b) Y-HfO_2, and (c) $Hf_{0.5}Zr_{0.5}O_2$, with electric field along [001] and [011] directions, respectively. The evolution of the free energy landscape with electric field is shown in SM Sec. V [22]. In the cases with $\boldsymbol{E}//[011]$, u represents the magnitude of the polar modes projected on the direction of the electric field. The color of the segment (red, blue, and green) indicates the state is in the local minimum corresponding to the tetragonal, oIII, oIV structure, respectively. For Y-HfO_2, the blue segment represents that the structure containing an oIII part.

first cusp value $u_z < 0.06$ Å, the energy as a function of u_z is very close to that of pure HfO_2. In both systems, with increasing u_z, A_y couples with u_z linearly and B_z remains zero. At the first cusp $u_z = 0.06$ Å, both A_y and B_z exhibit boosts, indicating a structural transformation with a change in symmetry. A representative structure with $u_z = 0.08$ Å is shown in Fig. 6(b). The supercell can be divided into two parts with distinct behavior. The unsubstituted part of the supercell has the atomic displacements characteristic of the polar oIII structure, which is responsible for the ferroelectricity. Here, the adjacent oxygen layers (indicated by the arrows) have different bonding environments. As a result, they are prone to have different displacements, leading to a nonzero B_z, which is the character of the oIII structure. The part of the supercell containing the Y atom is less distorted. At the second cusp $u_z = 0.10$ Å, there is a downward jump in B_z, indicating another phase transition. Figure 6(b) shows the structure of the polar phase at $u = u_{\min} = 0.18$ Å. The structure in the unsubstituted part of the supercell closely resembles the polar oIII structure, while the part of the supercell containing the Y atom is close to the oIV phase. The decrease in B_z is attributed to the formation of the oIV phase in the Y-substituted part, with zero B_z as indicated in Fig. 3(c).

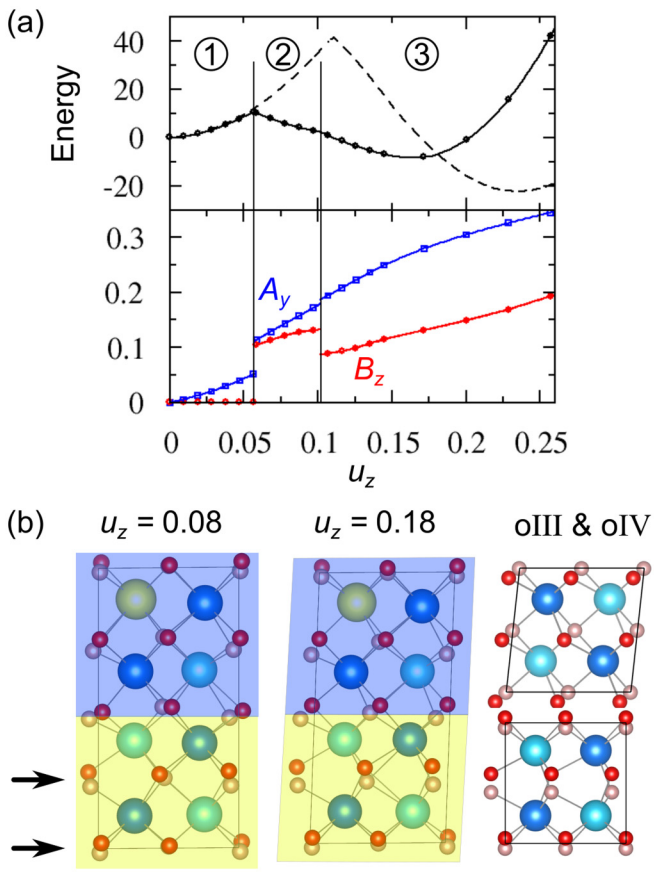

FIG. 6. (a) Energy of Y-HfO_2 as a function of u_z with other degrees of freedom relaxed. The same profile for pure HfO_2 is also plotted (dashed line) for comparison. (b) Crystal structure of Y-HfO_2 for $u_z = 0.08$ and 0.18 Å. The structures of the oIII and oIV phase in pure HfO_2 are also shown for comparison.

Relative to pure HfO_2, both the value of u_z at the cusp and the height of the energy barrier in Y-HfO_2 are lower, indicating a smaller critical electric field $E_{T\to P}$ for triggering the tetragonal to polar phase transition. The behavior in applied electric field exhibits corresponding differences. The detailed evolution of the free energy landscape with electric field is shown in Fig. S6 [22]. Here, because of the added hole, the density of states at the Fermi level is nonzero and we investigate the change of structure under an electric field with an accompanying nonzero field-induced current. As shown in Fig. 5(b), for E//[001], the critical field $E_{T\to P} = 9.0$ MV/cm for the transition from the tetragonal to the polar phase is much reduced compared with that [$E_{T\to P} = 15.0$ MV/cm] in pure HfO_2, as expected from the lower barrier. Furthermore, the saturation polar distortion is smaller than in pure HfO_2.

Figure 7 shows the energy profile of Y-HfO_2 as a function of $u = u_y = u_z$. For small u, A_y couples with u_z linearly while B_z remains approximately zero, very close to the behavior in pure HfO_2. Similar to the energy profile of Y-HfO_2 along the

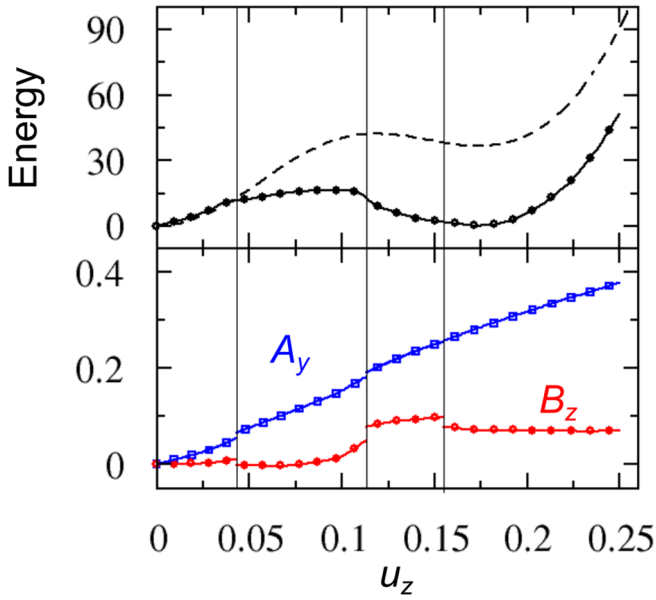

FIG. 7. Energy, A_y, and B_z as a function of u_z along the path of the tetragonal to oIV phase transition. Along this transformation path, u_y is fixed to be equal to u_z. The representative structures of each intermediate states are shown in Fig. S3 [22].

[001] direction, Y doping also introduces intermediate states, here two rather than one, and the phase changes along the transformation path are indicated by the singular points of the B_z profile (see SM Fig. S3 for the representative structure of each intermediate state [22]). Even though the relative energy of the oIV structure is lowered in Y-HfO_2, we see that the curvatures of the local minima, which correlate to the maximum slopes in the energy profile, are approximately the same as those in pure HfO_2, indicating that the critical fields for inducing the phase transitions are similar [Figs. 5(a) and 5(b)].

C. $Hf_{0.5}Zr_{0.5}O_2$

The energy landscape of $Hf_{0.5}Zr_{0.5}O_2$ as a function of the two polar mode amplitudes u_y and u_z is shown in Fig. 8(a). As in pure HfO_2, there are local minima corresponding to the tetragonal and oIII phases. However, the cation layering normal to the y direction breaks the y-z symmetry of pure HfO_2, so the two local minima for oIII, with polarization in the y direction and polarization in the z direction, respectively, are not equivalent. In addition, the polar distortion of z-polarized oIII polarized in the z direction has a small nonzero y component, which resulting in two symmetry-related variants, one with positive y component and one with negative y component. We also see that in $Hf_{0.5}Zr_{0.5}O_2$, the oIV phase is unstable. Structural optimization starting from an oIV structure leads to the oIII minimum, as shown in Fig. 8(a).

In Fig. 8(b), we plot the energy of $Hf_{0.5}Zr_{0.5}O_2$ as a function of u_z, with the amplitudes of other modes at their optimized values, shown in Figs. 8(a) and 8(b). As in pure HfO_2, this energy profile also exhibits two local minima corresponding to the tetragonal and oIII phases, very little changed from the pure case. However, the cusp seen in pure HfO_2 is cut

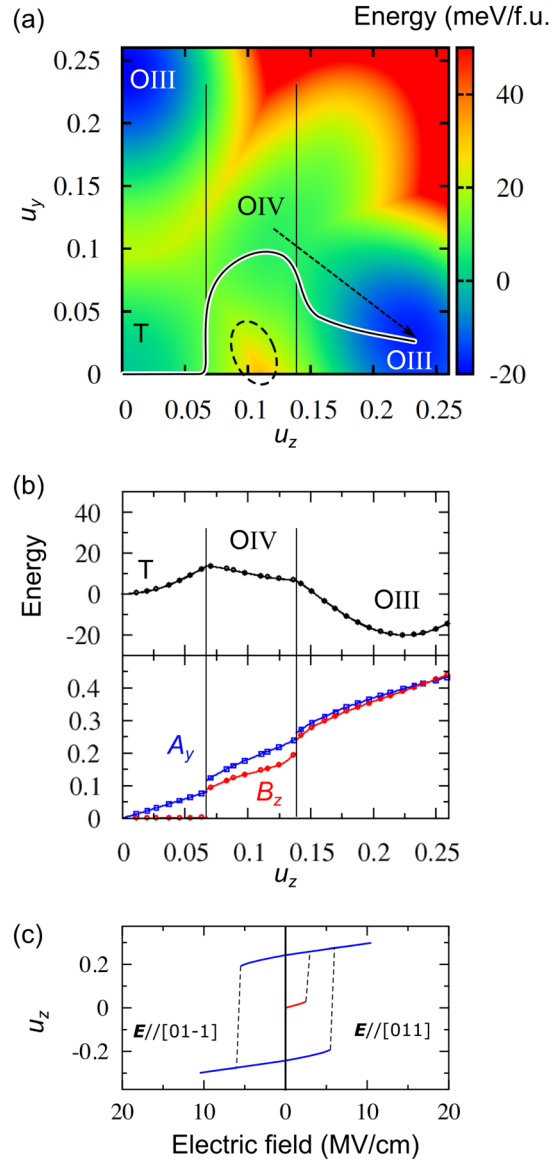

FIG. 8. (a) Energy landscape of $Hf_{0.5}Zr_{0.5}O_2$ with respect to the amplitudes of the u_y and u_z polar modes. (b) Energy profiles of $Hf_{0.5}Zr_{0.5}O_2$ as a function of u_z with energy minimized with respect to u_y. The values of u_y at each u_z are shown by the black curve with a white edge in (a). The values of A_y and B_z at each u_z are shown in the lower panel. (c) Hysteresis loop in which the forward electric is along the [011] direction and the backward one is along [01-1].

off, substantially lowering the energy barrier between the two phases. The lowering of the energy barrier results from the change in the path through the energy landscape, which goes through the oIV phase region and around the peak between the tetragonal and oIII phase [see Fig. 8(a)]. This is in contrast to pure HfO_2, in which the optimal path runs along the horizontal axis.

These features significantly influence the electric-field cycling behavior of $Hf_{0.5}Zr_{0.5}O_2$. As shown in Fig. 5(c), both [001] and [011] directed electric fields induce a transition from the tetragonal phase to the z-polarized oIII phase, with the critical field $E_{T\to P}$ being much smaller if E is applied

along the [011] direction (3.0 MV/cm vs 10.5 MV/cm). Furthermore, the hysteresis loop for $\boldsymbol{E}$//[011] exhibits a complex and unconventional shape. Once an [011]-directed electric field has induced the tetragonal to z-polarized oIII phase transition, the system stays trapped in the local oIII minimum as the field is increased to $E = 10.5$ MV/cm and then decreased. However, when the electric field in the reverse direction reaches $E = -12.0$ MV/cm, the polar distortion switches to the [011] direction to align with the field driving the system into the oIV phase polarized in the $[0\bar{1}\bar{1}]$ direction. As the magnitude of the field is decreased, the system remains trapped in the local oIV minimum until the field reaches -0.5 MV/cm, at which point the system switches back to the oIII phase with polar distortion in the negative z direction. In Fig. S8, we show this in more detail, connecting the complexity in the hysteresis loop of $Hf_{0.5}Zr_{0.5}O_2$ to the specific features of its energy landscape [22].

The surprising fact that the critical field for switching to the oIII phase is lower along [011] than along the polarization direction [001] is related to the complexity of the energy landscape. Indeed, an electric field along $[01\bar{1}]$ is also more effective in driving the state out of the oIII minimum, compared with a $[00\bar{1}]$ or $[0\bar{1}\bar{1}]$ oriented one. In Fig. 8(c), we show the polar mode amplitude hysteresis loop for an electric field cycle in which the field is first increased from zero along [011], decreased to zero, and then increased along $[01\bar{1}]$. Because the energy landscape is the same under $u_z \rightarrow -u_z$, the hysteresis loop is symmetrical. The magnitude of the coercive field for flipping the polar distortion is 5.5 MV/cm, smaller than those (10.5 and 12.0 MV/cm) with electric field along [001] and [011] directions. These results open possibilities for improving the electrical performance of HfO_2 by modulating the direction of applied electric field.

We note that the results we have presented are based on calculations with the LDA functional. Both LDA and GGA functionals have been used in previous first-principles studies of these materials [16,29–32]. Using the generalized gradient approximation (GGA) changes the relative energy of each phase (see SM Sec. I, Table S4 [22]) but does not destabilize any of the phases we considered. Therefore, the energy landscapes generated by GGA possess the same multiple local minima, with an electric field similarly inducing phase transitions between them. The Born effective charges given by the two different functionals are listed in the SM Sec. I Table S5 [22]. The tensor components given by LDA and GGA are similar in the tetragonal and oIII phases, but differ in the oIV one, especially for the off-diagonal elements. This will lead to some quantitative changes in the critical fields and polar distortion values in the calculated hysteresis loops.

IV. DISCUSSION

We have demonstrated that the tetragonal phase of HfO_2 can transform to the ferroelectric oIII or oIV phase under an electric field, providing insights into the emergence of ferroelectricity and electric-field-cycling behaviors. In the following subsections, we will relate our computational results to experimental observations.

A. Wake-up and ferroelectricity

The wake-up effect, which refers to the fact that an as-grown HfO_2-based thin film needs several electric field cycles to establish its full value of switching polarization, has been widely observed in experiments [33–36]. This wake-up effect has been attributed to various factors, including structural change at the interface [34,35,37], and the internal bias fields caused by oxygen vacancies [38–40].

In addition, an electric-field-induced nonpolar to polar phase transition is expected to play a significant role [34,41–43]. In experiments, doped HfO_2 films are usually deposited at high temperature [3–5,9]. High temperature, surface energy, and dopants all promote the formation of the tetragonal phase [28,44]. Upon cooling, the thin films can be kinetically trapped in the tetragonal phase, since it is metastable, with no unstable phonon modes [13]. However, the oIII structure has a lower energy than the nonpolar tetragonal phase, so that once the more stable oIII structure is induced by an electric field, a electric field opposite to the polarization will tend to flip the polarization to the corresponding oIII phase rather than drive the system back to the tetragonal phase.

In our calculations, for pure HfO_2 the critical electric field $E_{T\rightarrow P}$ for triggering this phase transition is 15.0 MV/cm. Our calculations also show that Y and Zr doping can cut off the cusp in the energy profiles by introducing intermediate states and thus lower the energy barrier and critical fields ($E_{T\rightarrow P} =$ 9.0 MV/cm in Y-HfO_2 and 3 MV/cm in $Hf_{0.5}Zr_{0.5}O_2$).

Moreover, we note that since the energy barriers are not very high, thermal vibration can facilitate the phase transition and further lower the critical fields. With the simple assumption that a phase transition will be driven by thermal vibration if (1) compared with the current state, the energy of another state is lower by more than $k_BT/2$ per formula unit, and (2) the energy barrier between the two states is lower than $k_BT/2$ per formula unit, we find that the critical fields are further reduced to 1.1 MV/cm (in Y-HfO_2) and 2.2 MV/cm (in $Hf_{0.5}Zr_{0.5}O_2$), which are the same order of magnitude as the experimental values [3,4,9].

B. Electrical hysteresis loops

The $Hf_{0.5}Zr_{0.5}O_2$ system with $\boldsymbol{E}$//[001] exhibits a conventional hysteresis loop with coercive field $E_c = 10.5$ MV/cm. In contrast, in pure HfO_2, we do not observe a complete hysteresis loop, due to the large energy barrier in the polar distortion flipping transformation path; this highlights the effect of substitution in lowering energy barriers to allow switching between competing phases.

The barrier-lowering effects of substitution are further illustrated by the behavior of other systems considered here. In a conventional ferroelectric hysteresis loop, the polarization jumps at the coercive field. However, in Fig. 5, we see that jumps in polar distortion can occur at two or more values of the electric field, leading to more complex hysteresis loops. This phenomenon has been discussed in Ref. [39] and referred as the 'split-up' effect. This 'split-up' effect has been attributed to the different activation energies in grains with different oxygen vacancy concentrations [39]. Here, we would like to point out that the competing phases in the energy landscape can also contribute to this effect. As shown in

Fig. 5, state hopping between different (tetragonal, oIII, and oIV) local minima can lead to multiple boosts. Moreover, our results demonstrate that electric field cycling behaviors are also field-direction dependent. In HfO_2-based thin films composed of multiple grains [35,36,45], grains with different lattice orientations may follow different transformation paths with different critical fields.

V. CONCLUSION

In this study, we investigated the energy landscapes of pure HfO_2, Y-doped HfO_2, and $Hf_{0.5}Zr_{0.5}O_2$ as a function of the polar modes u_y and u_z. The complex energy landscapes of these systems are found to possess multiple local minima, corresponding to the tetragonal, oIII, and oIV phases, respectively. Moreover, we find that Y and Zr doping can lower the energy barriers between the nonpolar tetragonal phase and the ferroelectric oIII phase, by introducing intermediate states. In $Hf_{0.5}Zr_{0.5}O_2$ with an ordered cation arrangement, the oIV phase becomes unstable, and a new transformation path for the tetragonal to oIII phase transition is opened, with a lower energy barrier. We connect our results to experimental observations, such as the wake-up effect and *P-E* loop with irregular shape, and also propose dependence of behavior on the direction of applied electric field. This work provides useful insights about the origin of the ferroelectric phase in HfO_2-based films and suggests strategies for improving their ferroelectric performance.

ACKNOWLEDGMENTS

We thank Sebastian E. Reyes-Lillo, Fei-Ting Huang, Xianghan Xu, and Sang-Wook Cheong for valuable discussions. This work was supported by Office of Naval Research Grant No. N00014-17-1-2770. Computations were performed by using the resources provided by the High-Performance Computing Modernization Office of the Department of Defense and the Rutgers University Parallel Computing (RUPC) clusters.

[1] M. T. Bohr, R. S. Chau, T. Ghani, and K. Mistry, IEEE Spectrum **44**, 29 (2007).
[2] M. Gutowski, J. E. Jaffe, C.-L. Liu, M. Stoker, R. I. Hegde, R. S. Rai, and P. J. Tobin, Appl. Phys. Lett. **80**, 1897 (2002).
[3] T. Böscke, J. Müller, D. Bräuhaus, U. Schröder, and U. Böttger, Appl. Phys. Lett. **99**, 102903 (2011).
[4] T. S. Böscke, S. Teichert, D. Bräuhaus, J. Müller, U. Schröder, U. Böttger, and T. Mikolajick, Appl. Phys. Lett. **99**, 112904 (2011).
[5] S. Mueller, C. Adelmann, A. Singh, S. Van Elshocht, U. Schroeder, and T. Mikolajick, ECS J. Solid State Sci. Technol. **1**, N123 (2012).
[6] S. Mueller, J. Mueller, A. Singh, S. Riedel, J. Sundqvist, U. Schroeder, and T. Mikolajick, Adv. Funct. Mater. **22**, 2412 (2012).
[7] J. Müller, T. Böscke, D. Bräuhaus, U. Schröder, U. Böttger, J. Sundqvist, P. Kücher, T. Mikolajick, and L. Frey, Appl. Phys. Lett. **99**, 112901 (2011).
[8] J. Müller, U. Schröder, T. S. Böscke, I. Müller, U. Böttger, L. Wilde, J. Sundqvist, M. Lemberger, P. Kücher, T. Mikolajick, and L. Frey, J. Appl. Phys. **110**, 114113 (2011).
[9] J. Muüller, T. S. Böscke, U. Schröder, S. Mueller, D. Bräuhaus, U. Böttger, L. Frey, and T. Mikolajick, Nano Lett. **12**, 4318 (2012).
[10] S. S. Cheema, D. Kwon, N. Shanker, R. Dos Reis, S.-L. Hsu, J. Xiao, H. Zhang, R. Wagner, A. Datar, M. R. McCarter, C. R. Serrao, A. K. Yadav, G. Karbasian, C.-H. Hsu, A. J. Tan, L.-C. Wang, V. Thakare, X. Zhang, A. Mehta, E. Karapetrova, R. V. Chopdekar, P. Shafer, E. Arenholz, C. Hu, R. Proksch, R. Ramesh, J. Ciston, and S. Salahuddin, Nature (London) **580**, 478 (2020).
[11] H.-J. Lee, M. Lee, K. Lee, J. Jo, H. Yang, Y. Kim, S. C. Chae, U. Waghmare, and J. H. Lee, Science **369**, 1343 (2020).
[12] J. Wang, H. P. Li, and R. Stevens, J. Mater. Sci. **27**, 5397 (1992).
[13] S. E. Reyes-Lillo, K. F. Garrity, and K. M. Rabe, Phys. Rev. B **90**, 140103(R) (2014).
[14] X. Sang, E. D. Grimley, T. Schenk, U. Schroeder, and J. M. LeBeau, Appl. Phys. Lett. **106**, 162905 (2015).
[15] M. H. Park, Y. H. Lee, H. J. Kim, Y. J. Kim, T. Moon, K. D. Kim, J. Müller, A. Kersch, U. Schroeder, T. Mikolajick, and C. S. Hwang, Adv. Mater. **27**, 1811 (2015).
[16] T. D. Huan, V. Sharma, G. A. Rossetti Jr., and R. Ramprasad, Phys. Rev. B **90**, 064111 (2014).
[17] P. Giannozzi, S. Baroni, N. Bonini, M. Calandra, R. Car, C. Cavazzoni, D. Ceresoli, G. L. Chiarotti, M. Cococcioni, I. Dabo, A. D. Corso, S. de Gironcoli, S. Fabris, G. Fratesi, R. Gebauer, U. Gerstmann, C. Gougoussis, A. Kokalj, M. Lazzeri, L. Martin-Samos, N. Marzari, F. Mauri, R. Mazzarello, S. Paolini, A. Pasquarello, L. Paulatto, C. Sbraccia, S. Scandolo, G. Sclauzero, A. P. Seitsonen, A. Smogunov, P. Umari, and R. M. Wentzcovitch, J. Phys.: Condens. Matter **21**, 395502 (2009).
[18] X. Gonze, J.-M. Beuken, R. Caracas, F. Detraux, M. Fuchs, G.-M. Rignanese, L. Sindic, M. Verstraete, G. Zerah, F. Jollet, M. Torrent, A. Roy, M. Mikami, P. Ghosez., J.-Y. Raty, and D. Allan, Comput. Mater. Sci. **25**, 478 (2002).
[19] http://opium.sourceforge.net
[20] J. W. Bennett, Phys. Procedia **34**, 14 (2012).
[21] H. J. Monkhorst and J. D. Pack, Phys. Rev. B **13**, 5188 (1976).
[22] See Supplemental Material at http://link.aps.org/supplemental/10.1103/PhysRevB.102.214108 for information regarding the computed structural parameters, descriptions about symmetry-adapted lattice modes, effective charges, constrained relaxations, intermediate states, and evolution of the energy landscapes under electric field. SM consists Refs. [13,16,24–26,30,46].
[23] S. L. Weeks, A. Pal, V. K. Narasimhan, K. A. Littau, and T. Chiang, ACS Appl. Mater. Interfaces **9**, 13440 (2017).
[24] X. Wang and D. Vanderbilt, Phys. Rev. B **75**, 115116 (2007).
[25] X. Wang and D. Vanderbilt, Phys. Rev. B **74**, 054304 (2006).
[26] L. Bellaiche, A. García, and D. Vanderbilt, Phys. Rev. B **64**, 060103(R) (2001).

[27] N. Sai, K. M. Rabe, and D. Vanderbilt, Phys. Rev. B **66**, 104108 (2002).
[28] C.-K. Lee, E. Cho, H.-S. Lee, C. S. Hwang, and S. Han, Phys. Rev. B **78**, 012102 (2008).
[29] J. E. Jaffe, R. A. Bachorz, and M. Gutowski, Phys. Rev. B **72**, 144107 (2005).
[30] X. Zhao and D. Vanderbilt, Phys. Rev. B **65**, 233106 (2002).
[31] R. Materlik, C. Künneth, and A. Kersch, J. Appl. Phys. **117**, 134109 (2015).
[32] K. Kamiya, N. Umezawa, and S. Okada, Phys. Rev. B **83**, 153413 (2011).
[33] D. Zhou, J. Xu, Q. Li, Y. Guan, F. Cao, X. Dong, J. Müller, T. Schenk, and U. Schröder, Appl. Phys. Lett. **103**, 192904 (2013).
[34] M. Pešić, F. P. G. Fengler, L. Larcher, A. Padovani, T. Schenk, E. D. Grimley, X. Sang, J. M. LeBeau, S. Slesazeck, U. Schroeder, and T. Mikolajick, Adv. Funct. Mater. **26**, 4601 (2016).
[35] E. D. Grimley, T. Schenk, X. Sang, M. Pešić, U. Schroeder, T. Mikolajick, and J. M. LeBeau, Adv. Electron. Mater. **2**, 1600173 (2016).
[36] D. Martin, J. Müller, T. Schenk, T. M. Arruda, A. Kumar, E. Strelcov, E. Yurchuk, S. Müller, D. Pohl, U. Schröder, S. V. Kalinin, and T. Mikolajick, Adv. Mater. **26**, 8198 (2014).
[37] M. Hoffmann, U. Schroeder, T. Schenk, T. Shimizu, H. Funakubo, O. Sakata, D. Pohl, M. Drescher, C. Adelmann, R. Materlik, A. Kersch, and T. Mikolajick, J. Appl. Phys. **118**, 072006 (2015).
[38] T. Schenk, M. Hoffmann, J. Ocker, M. Pešić, T. Mikolajick, and U. Schroeder, ACS Appl. Mater. Interfaces **7**, 20224 (2015).
[39] T. Schenk, U. Schroeder, M. Pešić, M. Popovici, Y. V. Pershin, and T. Mikolajick, ACS Appl. Mater. Interfaces **6**, 19744 (2014).
[40] C. Mart, K. Kühnel, T. Kämpfe, M. Czernohorsky, M. Wiatr, S. Kolodinski, and W. Weinreich, ACS Appl. Mater. Interfaces **1**, 2612 (2019).
[41] M. Hoffmann, U. Schroeder, C. Künneth, A. Kersch, S. Starschich, U. Böttger, and T. Mikolajick, Nano Energy **18**, 154 (2015).
[42] M. H. Park, H. J. Kim, Y. J. Kim, Y. H. Lee, T. Moon, K. D. Kim, S. D. Hyun, and C. S. Hwang, Appl. Phys. Lett. **107**, 192907 (2015).
[43] R. Batra, T. D. Huan, J. L. Jones, G. Rossetti Jr., and R. Ramprasad, J. Phys. Chem. C **121**, 4139 (2017).
[44] R. Batra, H. D. Tran, and R. Ramprasad, Appl. Phys. Lett. **108**, 172902 (2016).
[45] M. Hoffmann, M. Pešić, K. Chatterjee, A. I. Khan, S. Salahuddin, S. Slesazeck, U. Schroeder, and T. Mikolajick, Adv. Funct. Mater. **26**, 8643 (2016).
[46] A. A. Demkov, Phys. Status Solidi B **226**, 57 (2001).